

Enhancing Electrical Properties and Seebeck Effects of WO₃ Thin Films Using Spray Pyrolysis: Insights into the Conductivity and Carrier Type

Zahra Asghari^{1 a}, Hamid Arian Zad^{2 b}, and Hosein Eshghi¹

¹ Physics Department, Shahrood University of Technology, Shahrood, Iran

² Alikhanyan National Science Laboratory, Alikhanian Br. 2, 0036 Yerevan, Armenia

the date of receipt and acceptance should be inserted later

Abstract. This study focuses on enhancing the electrical and thermoelectric properties of tungsten trioxide (WO₃) thin films using the spray pyrolysis technique. Three samples, namely A₁, A₂, and A₃, were prepared by depositing the films onto glass substrates at different deposition rates: R₁ = 1 mL/min, R₂ = 3 mL/min, and R₃ = 7 mL/min, respectively. Subsequently, the films underwent annealing at 500 °C for 2 hours in air. A detailed investigation was conducted to analyze the structural, morphological, optical, and electrical properties of the WO₃ thin films. The FE-SEM images revealed the formation of circular strings with varying diameters for all layers. The diameter of each string decreased as the deposition rate increased. XRD structural analysis indicated that, before annealing, sample R₁ exhibited a polycrystalline nature with mixed tetragonal-hexagonal phases, while the other two samples were amorphous. After annealing, sample A₃ also became polycrystalline. Moreover, the UV-Vis spectra analysis demonstrated a monotonic decrease in the band gap of the layers with increasing spray rate, potentially attributed to the attenuation of the quantum confinement effect. The Seebeck effect was used to authenticate the *n*-type conductivity of the WO₃ layers, as the Seebeck effect and conductivity exhibited a direct connection. Furthermore, the current-voltage variation was found to align with the oxygen vacancies sites. Remarkably, the sample A₃ with the highest deposition rate exhibited the lowest resistivity.

PACS. –

Keywords: Tungsten trioxide WO₃; Seebeck effect; Thermoelectrical properties

1 Introduction

Semiconductor characterization plays a crucial role in the advancement of semiconductor technology. Among the intermediate metal oxides, tungsten trioxide (WO₃) stands out as a widely studied *n*-type semiconductor with a large indirect band gap of approximately 2.4-3.7 eV [1–6]. Its optoelectronic properties have attracted considerable attention for potential applications such as smart windows [5–7], front contacts in photovoltaic solar cells [8–10], and variable-reflectance mirrors [11, 12].

Thin films of WO₃ have recently gained significant prominence due to their excellent electrochemical stability, making them ideal for use as photo-anodes in photo-electrochemical cells [13–17]. There are other works that provide insights into the fabrication techniques, properties, performance enhancement strategies, and potential applications of WO₃ thin films in the field of gas sensing [18, 19]. Previous studies have reported the intrinsic reaction mechanism of WO₃/electrolyte interfaces in various

electrolytes [20–23]. The deposition of WO₃ thin films has been achieved through various techniques, including physical vapor deposition (PVD), chemical vapor deposition (CVD) [24], evaporation [25–27], electrodeposition [28], sputtering [29–32], sol-gel deposition [27, 33], and spray pyrolysis technique [34–37]. The latter technique presents many advantages such as: (i) short time deposition, (ii) simple technology, (iii) low-cost, (iv) no need for vacuum, and (v) large scale area of thin film production.

Many researchers have devoted themselves to studying WO₃ thin films prepared under different spray rates [28] and the effect of annealing on the structural, surface morphological, and optical properties of WO₃ thin films [25, 29, 33, 38, 39]. For example, the *p*-type conductivity of WO₃ thin films has been considerably investigated [24]. The materials were deposited by spray pyrolysis using a precursor tungsten hexachloride dissolved in ethanol. The authors of the same reference sagely considered parameters such as deposition temperature and pressure of the carrier gas as typical variables, resulting in enhanced optical and electrical properties of the WO₃ thin films. The influences of deposition parameters on surface

^a e-mail: zahraasghary42@yahoo.com

^b e-mail: arianzad.hamid@yepphi.am

morphology, conductivity, and optical and electrochromic properties were studied using X-ray diffraction (XRD), current-voltage measurements ($I - V$), UV-Vis spectrometry, and other techniques [24].

The Seebeck effect, also known as the thermoelectric effect, is of great interest in semiconductor physics, as it allows for the determination of the type of dominating charge carriers in a material and the relative position of the Fermi level with respect to the transport level. Phenomenologically, the Seebeck effect can be understood as a temperature gradient-induced voltage generation due to the shift in the energetic distribution of free charge carriers in a metal or semiconductor. However, the investigation of the Seebeck effect in WO_3 has been relatively limited.

In this paper, we present a detailed investigation of the Seebeck effect in WO_3 thin films. Our study focuses on three different samples, examining the thermoelectrical properties of WO_3 and shedding light on the anomalous behavior of this fascinating material under different deposition rates and annealing conditions. We verify the influence of the deposition rate and annealing process on various physical properties of the WO_3 thin films, including conductivity, optical properties, and electrical behavior. Furthermore, we analyze the correlation between variations in the Seebeck effect and changes in the aforementioned properties across the different samples. Through this comprehensive analysis, we aim to gain a deeper understanding of the thermoelectrical properties of WO_3 and provide valuable insights for its potential applications [24, 25, 28, 29, 33, 38, 39].

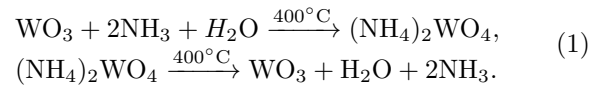
2 Experimental Procedure: General Information

The deposition of WO_3 thin films on glass substrates was carried out using the spray pyrolysis method. The precursor solution consisted of 50 mL of ammonium tungstate $[(\text{NH}_4)_2\text{WO}_4]$, prepared by dissolving pure WO_3 powder (99.9%, Merck) in a mixture of ammonia and distilled water. Three different spray rates, denoted as $R_1 = 1$ mL/min, $R_2 = 3$ mL/min, and $R_3 = 7$ mL/min, were used for the deposition. The other deposition parameters, including the spray solution volume, nozzle-to-substrate distance, and substrate temperature, were maintained at 50 mL, 30 cm, and 400 °C, respectively.

Prior to deposition, all substrates underwent a cleaning procedure. They were washed with soap and water, followed by immersion in a container containing acetone and distilled water. Subsequently, the substrates were placed in an ultrasonic machine for 16 minutes. Finally, the substrates were rinsed with deionized water and dried using nitrogen gas.

The preparation of transparent WO_3 thin films involved two steps. In the first step, a solution of ammonium tungstate $[(\text{NH}_4)_2\text{WO}_4]$ was sprayed onto the preheated substrates (at 400°C) using air as a gas conveyor. The experimental setup for the spray deposition process has been previously described in Ref. [40–42]. The resulting

films exhibited transparency, amorphous structure, homogeneity, and good adhesion to the substrate. In the second step, the sprayed films were annealed in ambient air. The annealing temperature was fixed at 500 °C, and the annealing time was set to 2 hours. The annealed films appeared transparent with a slightly yellowish color. The deposition of the WO_3 thin layer followed the chemical reactions [43]:



The morphologies of the samples were investigated using a Field Emission Scanning Electron Microscope (FE-SEM) (SIGMA 300-HV, Carl Zeiss). The structural characterization of the films was performed using X-ray diffraction (XRD) with CuK_α radiation (wavelength of 1.54 Å) and an angular range of 2θ from 10 to 70 degrees (XRD; Bruker AXS). The transmittance spectra of the studied samples were measured using a UV-Vis spectrophotometer (Shimadzu UV-Vis 1800) in the wavelength range of 300 – 1100 nm. The film thickness was determined using a Taylor/Hobson profile meter with an accuracy of +20 nm.

3 Results and discussion

The Seebeck effect, also referred to as the thermoelectric effect, is a phenomenon that occurs when there is a temperature difference across a conductor, such as a metal or semiconductor, resulting in the generation of an electric voltage. This effect is based on the behavior of charge carriers, such as electrons or holes, in response to temperature gradients. When a temperature gradient is applied to a conductor, meaning one end is heated while the other end is cooled, the charge carriers experience an imbalance in their distribution. Due to their thermal energy, the charge carriers diffuse from the hotter region to the colder region, seeking equilibrium. As a result, an accumulation of charge occurs at both ends of the conductor, creating an electric field. The electric field gives rise to a potential difference or voltage between the two ends of the conductor, which can be measured as the Seebeck voltage. This voltage is directly proportional to the temperature difference across the conductor. Hence, a larger temperature gradient will result in a higher Seebeck voltage. The Seebeck effect is fundamental to thermoelectric devices, which utilize this phenomenon to convert heat energy directly into electrical energy or vice versa. These devices, known as thermoelectric generators or thermoelectric coolers, find applications in various fields, including power generation, waste heat recovery, and temperature control systems.

Overall, the Seebeck effect demonstrates the conversion of a thermal gradient into an electric potential, highlighting the interconnected nature of temperature and electrical phenomena in conductive materials.

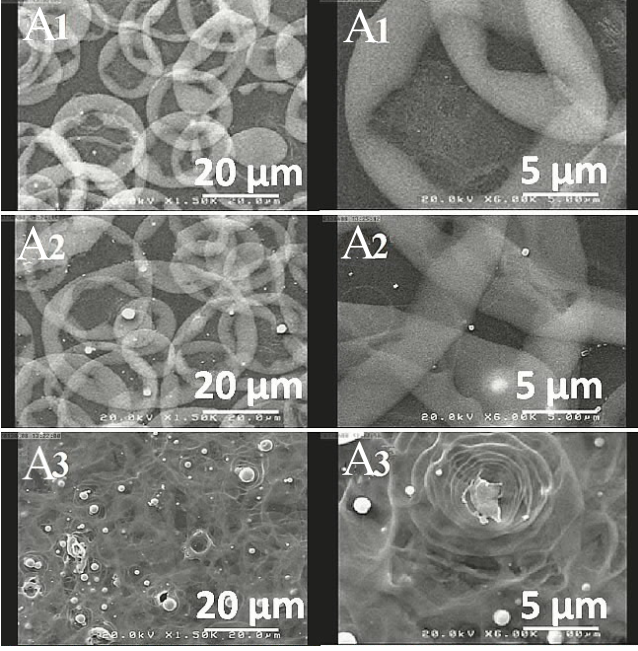


Fig. 1. The FE-SEM images of the prepared WO_3 samples are shown at three different spray rates: $R_1 = 1$ mL/min, $R_2 = 3$ mL/min, and $R_3 = 7$ mL/min, as depicted in Figure 1.

3.1 Non-annealed characterization of the WO_3 layers

3.1.1 Surface morphology: FE-SEM analysis

Figure 1 displays FE-SEM images of the grown samples A_1 , A_2 , and A_3 with their corresponding rates R_1 , R_2 , and R_3 , captured at two scales: $20 \mu\text{m}$ and $5 \mu\text{m}$. The FE-SEM images reveal that all samples are coated with numerous flat thin layers, forming spiral strings with rotating clusters known as lattice tungsten filaments. Notably, the presence of tungsten filaments with varying diameters is evident in all layers. The diameter of these filaments decreases with an increase in the deposition rate.

3.1.2 Structural properties

The XRD patterns of the studied layers are shown in Figure 2. Upon inspecting this figure, it is evident that the sample with the lowest deposition rate, R_1 , exhibits a polycrystalline nature. It consists of both tetragonal and hexagonal phases, with lattice parameters of $a = b = 23.33 \text{ \AA}$ and $c = 3.79 \text{ \AA}$ for the tetragonal phase, and $a = b = 7.29 \text{ \AA}$ and $c = 3.89 \text{ \AA}$ for the hexagonal phase. The patterns were indexed using SigmaPlot software, and it was observed that all peaks were in good agreement with the hexagonal structure of WO_3 by utilizing the standard data (JCPDS No. 05-0392) [44]. On the other hand, the samples grown at higher deposition rates, R_2 and R_3 , appear to be in the amorphous phase. Using theoretical analysis associated with the crystalline structure, it is possible to deduce the distance between adjacent planes and

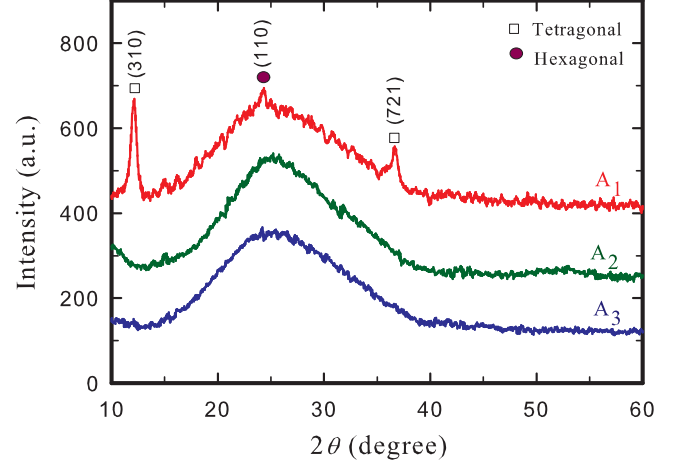


Fig. 2. The XRD spectra of studied WO_3 thin layers. The sample A_1 possessing the lowest deposition rate R_1 has been grown with a polycrystalline nature in a mixed tetragonal and hexagonal phases. Other samples were grown in amorphous phase.

the crystallite size in the grown samples. The distance between crystal planes, denoted as $d(hkl)$, can be obtained using Bragg's formula.

$$d_{(hkl)} = \frac{n\lambda}{2 \sin \theta}. \quad (2)$$

Accordingly, the crystallite size corresponding to a given Bragg's angle θ can be found using Scherer's equation.

$$D = 0.9 \frac{\lambda}{\beta \cos \theta}, \quad (3)$$

where λ is the X-ray wavelength and β is the full width at half maximum (FWHM) of the given peak. By using Equation (3), for the (310) peak positioned at the Bragg's diffraction angle of $\theta \approx 12^\circ$, the crystallite size of sample A_1 is estimated to be around 16 nm. Additionally, the dislocation density δ of the sample can be calculated using the formula $\delta = 1/D^2$ [45] (for more information, see Table 1).

3.1.3 Electric and thermoelectric properties

The measurement tool description of the Seebeck effect for electric and thermoelectric properties is given as follows. A metal-semiconductor connection can be established to investigate the conductivity of the sample using

Table 1. Crystallite size, distance between crystal planes, strain, and density of dislocations in sample A_1 were analyzed.

Sample	$D(\text{nm})$	$d_{hkl}(\text{nm})$	$\varepsilon(\times 10^{-3})$	$\delta(\times 10^{-3})(\text{nm})^{-2}$
A_1	15.93	0.733	2.17	3.9

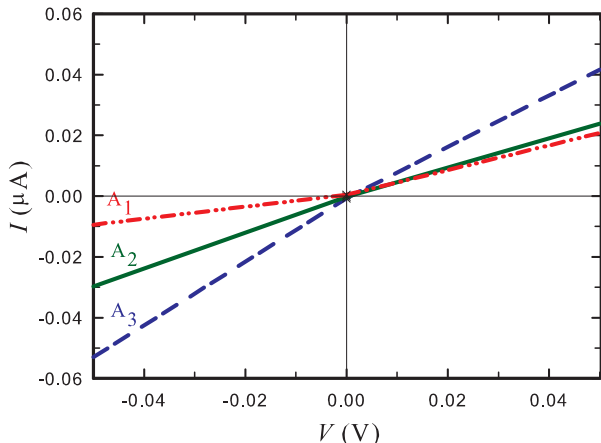


Fig. 3. The $I - V$ curves of the three studied samples are depicted in Figure 3. The plots exhibit a clear ohmic behavior, indicating that the samples follow Ohm's law.

an electroaccumulation device. This device offers different modes, including Cyclic Voltammetry (CV), Structure Porous Carbon (CPC), Hydrothermal Carbon (CHC), and extra [46]. In our study, we specifically employed the CV mode. The device settings involve defining a potential range from E_1 to E_2 and determining the number of steps for this scanning process as well as the repetitions of this potential cycle. Subsequently, by connecting the electrical terminals of the device to the output terminals of the component and applying voltage within a specific range, we measure the current flowing through the sample.

Figure 3 illustrates the current-voltage curves of the samples under investigation. The plots clearly demonstrate that all samples exhibit an ohmic behavior, and the resistivity of the layers decreases as the spray rate increases. To further elaborate on this phenomenon, we provide the following explanation. The sheet resistance, denoted as R_{sh} , can be determined by the ratio of voltage (V) to current (I), while the resistivity of the layers (ρ) is obtained from the relation $\rho = R_{sh}t$, where t represents the thickness of the layer. In our measurements, these quantities were evaluated for a $1 \times 1 \text{ cm}^2$ area of the samples. Figure 4(a) displays the resistivity variations of the studied layers. The plot reveals a significant decrease in resistivity from $71.3 \text{ } \Omega\text{-cm}$ for R_1 to approximately $18.8 \text{ } \Omega\text{-cm}$ for R_3 , which corresponds to the highest spray rate. This decrease in resistivity can be attributed to an increase in the density of oxygen vacancies within the network layer as the spray rate increases.

To determine the type of conductivity (either n -type or p -type) exhibited by the samples, we employed the Seebeck effect relation $\mathcal{V} = S\Delta T$ [47], where S is the Seebeck coefficient, \mathcal{V} is the thermoelectric power, and ΔT is the temperature difference across the width of the sample. The experimental results for the Seebeck effect are presented in Fig. 4(b).

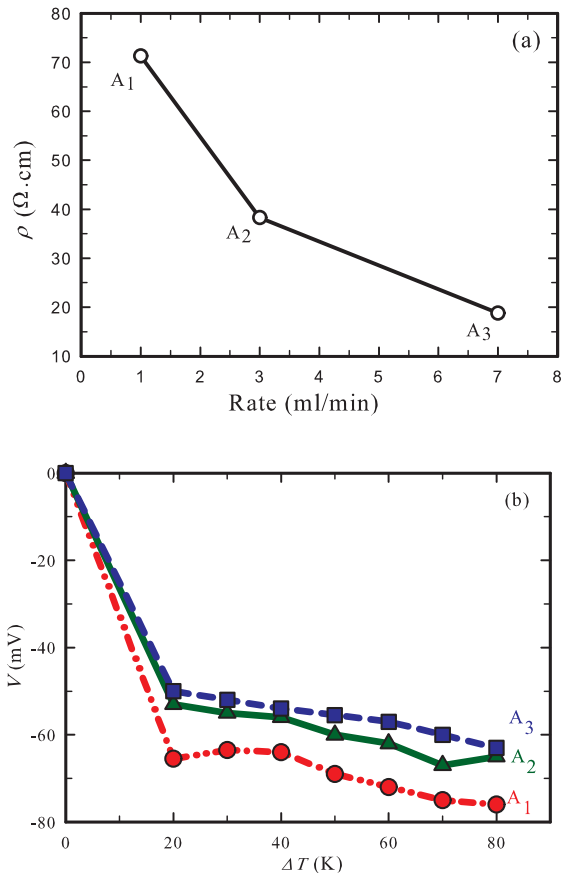


Fig. 4. (a) The dependence of the electrical resistivity on the spray rate for the samples prepared using a subtractive process. The plot clearly shows a decrease in resistivity as the spray rate increases. This trend can be attributed to an increase in the density of oxygen vacancies within the network layer. (b) The experimental data of the Seebeck effect in the studied samples. The Seebeck coefficient, which is determined by the majority of carriers, indicates the type of conductivity exhibited by the samples. In this case, all layers exhibit n -type conductivity. The temperature difference across the width of the samples was fixed at $\Delta T = 10^\circ\text{K}$ during the measurements.

Based on these results, it can be concluded that the Seebeck coefficient of the samples is negative, indicating n -type conductivity. Previous studies have reported an inverse proportionality between the Seebeck coefficient and the conductivity of the layer [48]. This finding is consistent with our obtained values from the $I - V$ data for the sheet resistance of the samples.

3.1.4 Optical properties

Figure 5 displays the UV-Vis. transmittance spectra of the non-annealed samples. In the visible region (around $t \approx 550 \text{ nm}$), the transmittance values are approximately 80% for A_1 , 70% for A_2 , and 30% for A_3 . These variations in transmission are consistent with the improvement

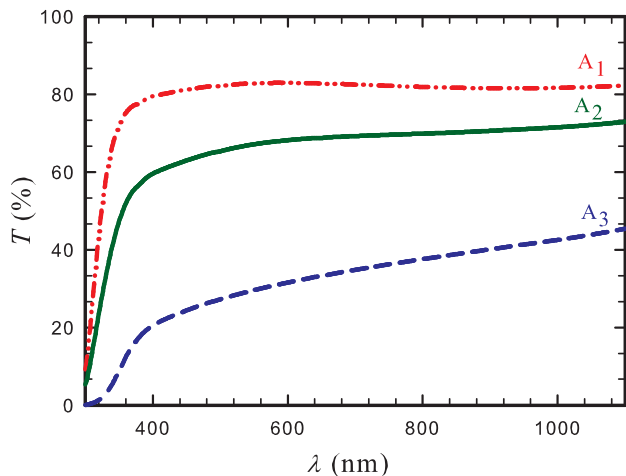


Fig. 5. The UV-Vis. transmittance spectra of the WO_3 films prepared under different spray rates ($1 \text{ mL/min} \leq R \leq 7 \text{ mL/min}$) are shown in Figure 5. The spectra illustrate the variation in transmittance across the UV and visible regions for the samples.

in the crystallinity of the layers and their thicknesses (approximately $t \approx 200 \pm 20 \text{ nm}$, $235 \pm 20 \text{ nm}$, and $290 \pm 20 \text{ nm}$ for the corresponding rates R_1 , R_2 , and R_3 , respectively). The observed changes in transmittance can be attributed to the reduction in photon scattering due to the better crystalline arrangement of the layers. As studied by M. Regragui *et al.* [34], the transmittance behavior is influenced by the annihilation of photon scattering, which is facilitated by the improved crystallinity in the layers. Consequently, we observe an enhancement in light transmission through the layers. Figure 6 depicts the spectra of the absorption coefficient of the samples as a function of wavelength λ , obtained using Lambert's equation.

$$\alpha = -\frac{\ln T}{t} \quad (4)$$

It is evident from this figure that all three samples exhibit relatively high absorption coefficients, approximately on the order of 10^4 cm^{-1} , in the ultraviolet region ($\lambda < 400 \text{ nm}$). Consequently, sample A_1 grown at rate R_1 displays a sharp absorption edge at 320 nm . As the spray rate increases, the absorption edge shifts towards longer wavelengths. By utilizing this information, we can determine the optical band gap E_g of the investigated films using the following formula: [49]

$$(\alpha h\nu)^m = A(h\nu - E_g), \quad (5)$$

Here, A represents a constant, $h\nu$ denotes the incident photon energy, and m depends on the nature of the band transition ($m = 2$ for direct transitions and $m = 1/2$ for indirect ones). The determination of both direct and indirect band gaps involves extrapolating the linear portion of the curve to the energy axis, specifically $(\alpha h\nu)^m = 0$. The analysis for the indirect band gaps is illustrated in detail

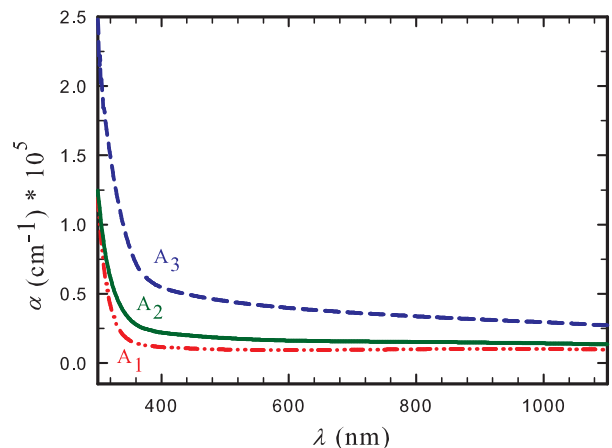


Fig. 6. The absorption coefficient as a function of wavelength λ . In the ultraviolet region ($\lambda < 400 \text{ nm}$), all samples exhibit high absorption coefficients, approximately on the order of 10^4 cm^{-1} .

in Fig. 7 (a), and the final results are presented in Fig. 7 (b). We observed that E_g increases from 3.11 to 3.51 eV as the spray rate decreases. These variations can be explained by the width of the distribution of defect states (mainly oxygen vacancies) near the conduction or valence band edges.

3.2 Annealed WO_3 layers characterization

3.2.1 Structural properties

WO_3 thin films were deposited on glass substrates using the spray pyrolysis technique at three different rates: $R_1 = 1 \text{ mL/min}$, $R_2 = 3 \text{ mL/min}$, and $R_3 = 7 \text{ mL/min}$. Subsequently, the films were annealed for 2 hours at 500°C in air. XRD structural analysis revealed that the sample A_2 grown at a rate of $R_2 = 3 \text{ mL/min}$ exhibited an amorphous nature, while samples A_1 ($R_1 = 1 \text{ mL/min}$) and A_3 ($R_3 = 7 \text{ mL/min}$) were found to be polycrystalline. Figure 8 displays the crystalline structure of thin films after annealing. It is noteworthy that before annealing two samples with rates R_2 and R_3 had an amorphous nature, while the sample A_1 with rate R_1 had polycrystalline monoclinic structure. As shown in Fig. 8 we see that after annealing samples A_1 and A_3 have polycrystalline structure, whereas the sample A_2 remains in the amorphous phase.

Interestingly, the sample A_1 is grown in three phases: monoclinic phase with lattice parameters $a = 14.49\text{\AA}$, $b = 14.50\text{\AA}$, $c = 10.92\text{\AA}$, hexagonal phase with lattice parameters $a = b = 7.28\text{\AA}$, $c = 3.88\text{\AA}$ and tetragonal phase with lattice parameters $a = b = 7.56\text{\AA}$, $c = 3.73\text{\AA}$. Moreover, A_3 sample is grown in the two aforescribed phases: monoclinic with lattice parameters $a = 14.49\text{\AA}$, $b = 14.50\text{\AA}$, $c = 10.92\text{\AA}$ and hexagonal with lattice parameters $a = b = 7.29\text{\AA}$, $c = 3.89\text{\AA}$ together with two new phases

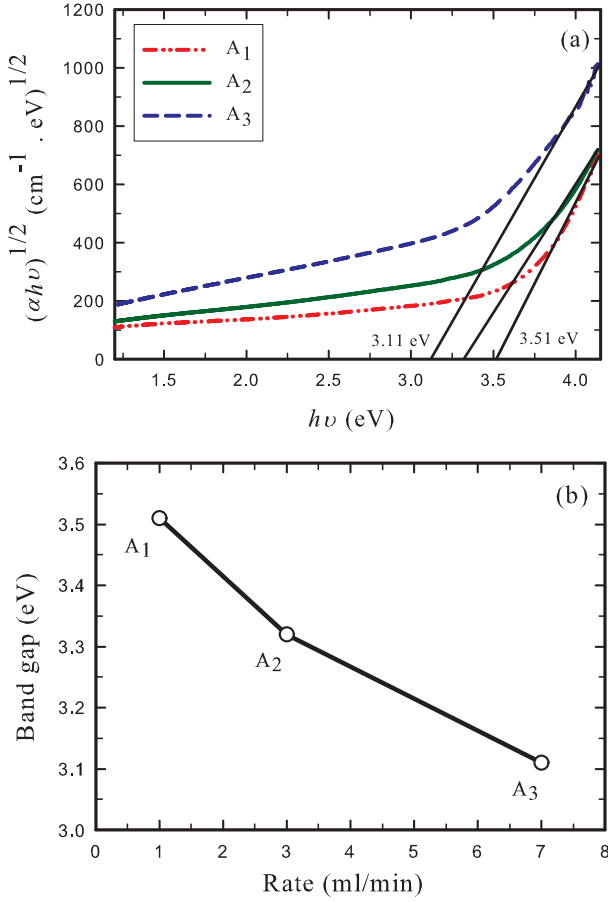


Fig. 7. The details of the band gap determination: (a) indirect band gaps (b) The final calculated results and variations of E_g .

so-called $(5(\text{NH}_4)_{20}).12\text{WO}_3$) and $((\text{NH}_4)_{0.42}\text{WO}_3)$. The preferential directions for both polycrystalline samples are grown along $(0\ 1\ 0)$ direction positioned at the Bragg angle of $\theta \approx 12^\circ$ (JCPDS 05-0392). Other researchers have reported the same results for example in Refs. [24, 50].

In order to further investigation of the obtained data, one can calculate crystal size, distance between network planes, strain and density of dislocation δ by implementing equations (2) and (3). Table 2 indicates that after annealing, the crystal size increases with an increase in the spray deposition rate, except for sample A_2 which remains in an amorphous phase. This phenomenon is consistent with the results reported in previous works [38, 51, 52]. It is worth noting that the distance between network planes is well-matched across the samples. It is interesting to mention

Table 2. Crystallite size, distance between the crystal planes, strain and the density of dislocation of planes in the samples A_1 and A_3 after annealing.

Sample	$D(\text{nm})$	$d_{hkl}(\text{nm})$	$\varepsilon(\times 10^{-3})$	$\delta(\times 10^{-3})(\text{nm})^{-2}$
A_1	30.66	0.804	1.14	1.06
A_3	39.42	0.814	0.87	0.64

that WO_3 exhibits unconventional behavior in the laboratory, and its structural properties studied by spray pyrolysis are unpredictable, resulting in either amorphous or crystalline structures. From the structural analysis results, we can calculate the strain $\varepsilon = \beta \cos(\theta)/4$ and the dislocation density $\delta = 1/D^2$ of the crystal plates [53]. The dislocation density represents the length of dislocation lines per unit volume of the crystal. Moreover, as the deposition rate increases, both the strain and the density of dislocations remarkably decrease, indicating improved crystallinity of the layers after annealing. This observation is consistent with the density of the $(0\ 1\ 0)$ peak [38, 51].

3.2.2 Electrical and Thermoelectric Properties

Figure 9 displays the $I-V$ curve of the studied samples after annealing. The sheet resistance R_{sh} of the layers decreases from $84\ \text{k}\Omega$ to $8.3\ \text{k}\Omega$, indicating an improved electrical conductivity. Additionally, we observe a decrease in resistivity ρ from $1.9\ \Omega\cdot\text{cm}$ to $0.26\ \Omega\cdot\text{cm}$, as shown in Figure 10 (a). The decrease in R_{sh} can be attributed to two reasons: firstly, the increase in carrier mobility, which depends on the dislocation density, and secondly, an increase in carrier density. The latter corresponds to an increase in acceptor concentration (tungsten vacancies/holes) relative to oxygen vacancies with an increase in both the spray deposition rate and annealing. [34, 48, 54–56]. The experimental results for the Seebeck effect of the samples after annealing are presented in Fig. 10 (b). The data clearly indicate that the majority of carriers in sample A_1 are electrons, indicating its n -type conductivity. On the other hand, samples A_2 and A_3 exhibit majority carriers as holes, indicating their p -type conductivity.

The observed conductivity types are a result of the deposition and annealing processes being performed in ambient air. During these processes, the surface of the WO_3 films can absorb oxygen, leading to the creation of tungsten vacancies with positive holes. The density of donor-like levels, particularly oxygen vacancies, decreases while the density of acceptor-like levels, specifically tungsten vacancies, increases. This phenomenon has been previously reported in the literature [57, 58].

It is known that the n -type conductivity of WO_3 is primarily attributed to the presence of oxygen vacancies, which are associated with non-stoichiometry in the WO_3 lattice. The balance between the dopant concentration and oxygen deficit influences the n -type conductivity of the WO_3 layers. In our case, the deposition and annealing in an oxidizing environment (air) result in the reduction of oxygen vacancies during the annealing process. This reduction contributes to the generation of positive holes, leading to a switch from n -type conductivity to p -type conductivity.

Furthermore, the highly oxidizing atmosphere can cause oxygen atoms to adsorb onto the surface of the WO_3 film, creating tungsten vacancies with six positive holes. This phenomenon is responsible for the p -type conductivity typically observed in WO_3 thin films [24].

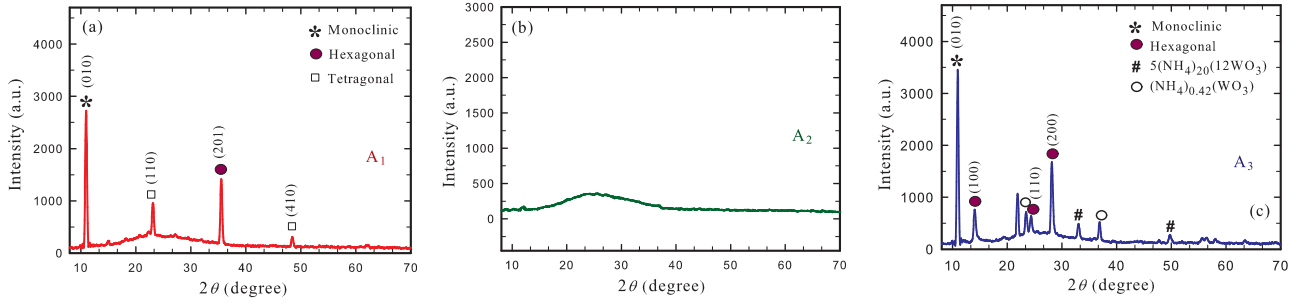


Fig. 8. XRD diagrams of WO_3 thin layers prepared at $T_R = 400^\circ\text{C}$ and subsequently annealed at $T_A = 500^\circ\text{C}$ are shown in (a) A_1 , (b) A_2 , and (c) A_3 . After annealing, A_1 and A_3 exhibit a polycrystalline structure, while A_2 remains in the amorphous phase.

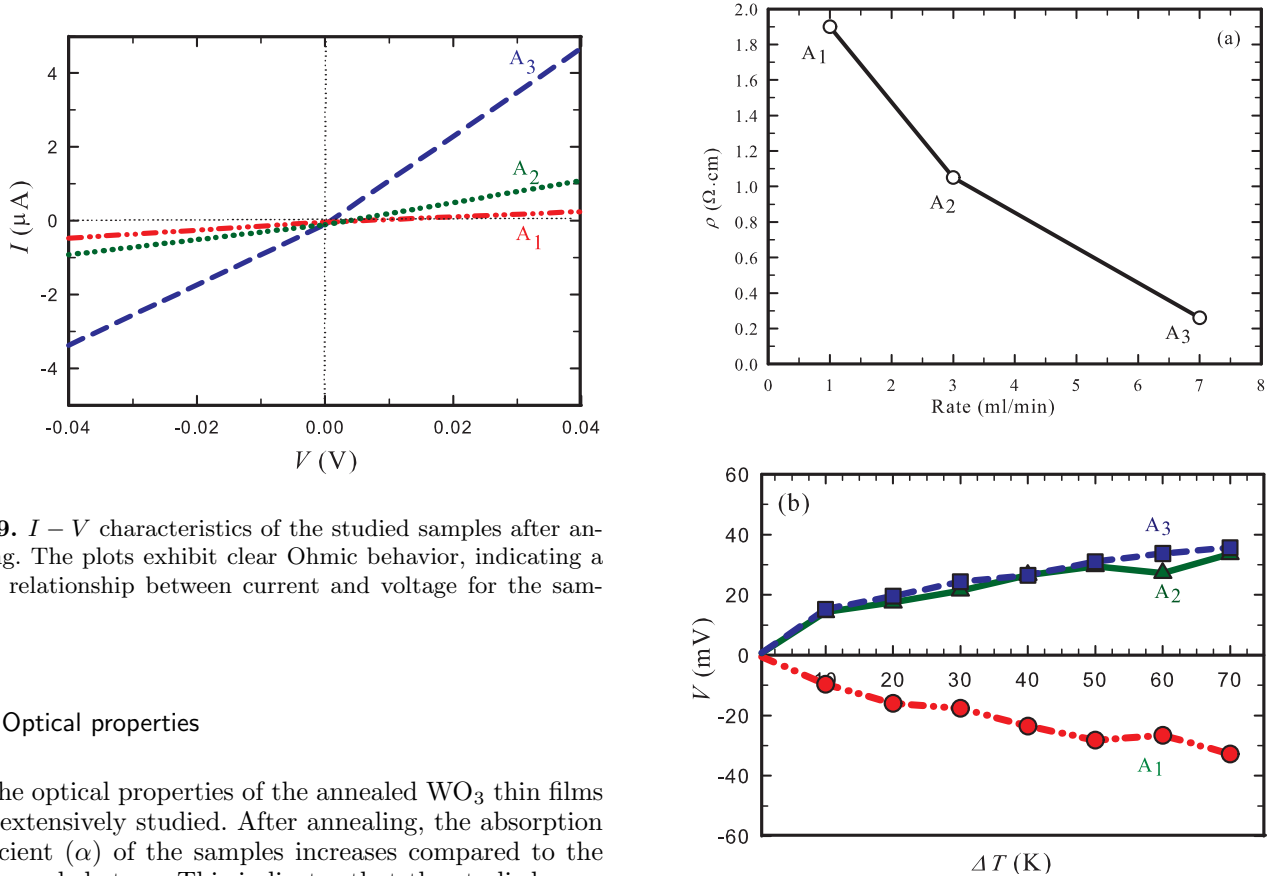


Fig. 9. $I - V$ characteristics of the studied samples after annealing. The plots exhibit clear Ohmic behavior, indicating a linear relationship between current and voltage for the samples.

3.2.3 Optical properties

The optical properties of the annealed WO_3 thin films were extensively studied. After annealing, the absorption coefficient (α) of the samples increases compared to the non-annealed stage. This indicates that the studied samples exhibit high absorbance properties ($\alpha \approx 10^5 \text{ cm}^{-1}$) in the ultraviolet wavelength region ($\lambda \leq 400 \text{ nm}$). Figure 11 illustrates the absorption as a function of wavelength (λ) for the annealed samples.

Using the absorption coefficient, we can straightforwardly determine the indirect optical band gap of the layers, as depicted in Figs. 12 (a) and (b). From these figures, it can be observed that the band gap of the considered layers decreases from 2.77 eV in A_1 to 2.50 eV in A_3 as the spray deposition rate increases.

The quantum confinement effect (QCE) describes electrons in terms of energy levels, potential wells, electron

Fig. 10. (a) Electrical resistivity of samples after annealing for 2 hours at 500°C . (b) Experimental data of the Seebeck effect. The temperature difference $\Delta T = 10^\circ\text{C}$ was maintained constant throughout the experiment.

energy band gaps, etc. It is observed when the size of the particle is too small to be comparable to the electron wavelength. WO_3 exhibits attractive properties due to the QCE caused by its small particle size (usually $< 10 \text{ nm}$) [59].

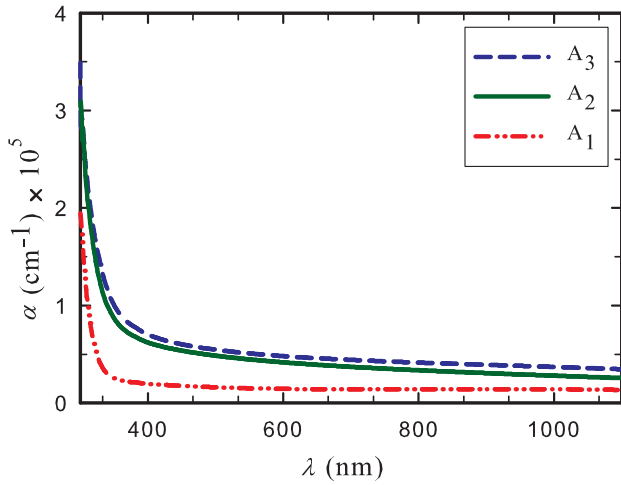


Fig. 11. The variation of absorption versus wavelength.

Furthermore, our investigations reveal that the reduction in band gap mentioned earlier is related to an increase in crystal size and may be attributed to the attenuation of the quantum confinement effect [48].

4 Conclusion

In this study, we investigated the influence of the deposition rate and annealing on the physical properties of WO_3 thin films prepared by the spray pyrolysis method. The FE-SEM images revealed the formation of circular strings with varying diameters, which decreased as the deposition rate increased. The XRD analysis indicated that sample A_1 exhibited a polycrystalline structure with mixed hexagonal-tetragonal phases.

Analysis of the optical data showed a decrease in the indirect band gap of the layers from 3.51 eV to 3.11 eV, attributed to changes in the width of the band tails of oxygen vacancies defect states near the band edges.

Regarding the Seebeck effect, our experimental results indicated that sample A_1 exhibited n -type conductivity, with electrons being the majority carriers, while samples A_2 and A_3 exhibited p -type conductivity, with holes being the majority carriers. After annealing, samples A_1 and A_3 exhibited crystallization in different structures. Additionally, the annealed films displayed a relatively high absorption coefficient of approximately 10^5 cm^{-1} and an indirect transition gap within the range of 2.50-2.77 eV for samples A_1 and A_3 . Furthermore, we observed that these materials exhibited n -type characteristics after annealing.

Based on our analysis, we have demonstrated the potential of the Seebeck effect as a useful experimental tool for determining the conductivity type of WO_3 under different conditions. As part of our future plans, we are currently conducting electrical measurements to optimize the resistivity of these thin films.

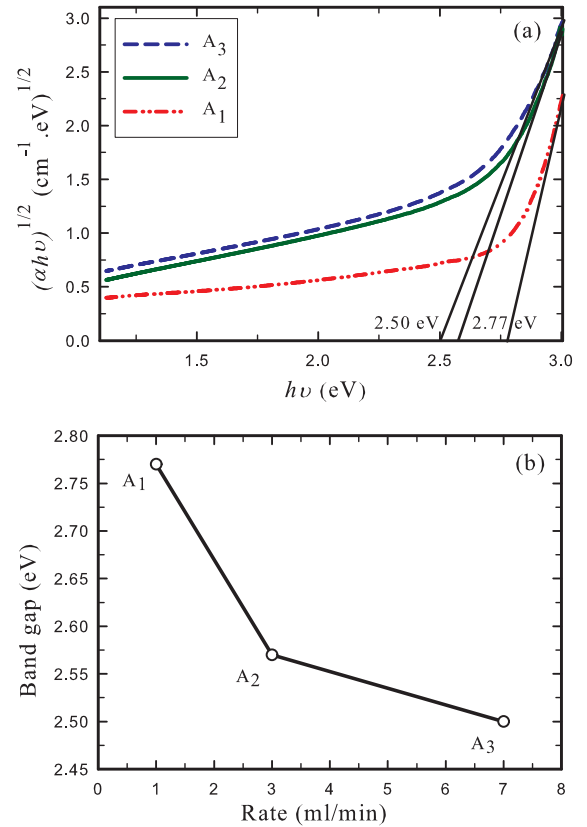


Fig. 12. (a) Indirect band gaps (E_g) calculated from the absorption coefficient of the layers. The spray deposition rate influences the indirect optical band gap of the layers. (b) Comparison of the indirect band gaps (E_g) for different spray deposition rates. The optical band gap of these layers decreases with an increase in the spray deposition rate.

Acknowledgements

Hamid Arian Zad acknowledges the receipt of the grant from the Abdus Salam International Centre for Theoretical Physics (ICTP), Trieste, Italy, and the CSMES RA in the frame of the research project No. SCS 19IT-008. H.A.Z also acknowledges for the financial support of the National Scholarship Programme of the Slovak Republic (NŠP).

Funding

This study was funded by ICTP and SAIA.

Conflicts of interest

The authors have no conflicts of interest to declare that are relevant to the content of this article.

Author contribution statement

All authors contributed equally to this work.

References

1. D. S. Dalavi, M. J. Suryavanshi, D. S. Patil, S. S. Mali, A. V. Moholkar, S. S. Kalagi, S. A. Vanalkar, S. R. Kang, J. H. Kim and P. S. Patil, *App. Surf. Sci.* **257**, 2647 (2011).
2. J. Zhang, X. L. Wang, X. H. Xia, C. D. Gu and J. P. Tun, *Solar Energy Materials & Solar Cells* **95**, 2107 (2011).
3. C. Y. Kim, S. G. Cho and T. Y. Lima, *Solar Energy Materials & Solar Cells* **93** 2056 (2009).
4. M. C. Rao, *Journal of Non-Oxide Glasses* **5**, 1 (2013).
5. A. Marques, L. Santos, S. Pereira, U. Emanuele, S. Sinopoli, R. Igreja, G. Sales, R. Martins and E. Fortunato. *Proceedings* **2**, 1065 (2018).
6. H. Qu, X. Zhang, H. Zhang, Y. Tian, N. Li, H. Lv, S. Hou, ; X. Li, J. Zhao, Y. Li, *Sol. Energy Mater. Sol. Cells* **163**, 23 (2017).
7. K. Mouratis, I. V. Tudose, C. Romanitan *et al.*, *Coatings* **12**, 545 (2022).
8. H. Razmi and R. M. Rezaei, *Electrochimica Acta* **56** 7220 (2011).
9. S. K. Gullapalli, R. S. Vemuri, F. S. Manciu, J. L. Enriquez, C. V. Ramana, *J. of Vac. Sci. and Tech. A Vac. Surf. and Film.* **28**, 824 (2010).
10. Y. Wang, I. Ramos and J. J. Santiago-Avilés, *J. of App. Phys.* **102**, 093517 (2007).
11. L. Wang and L. Zan, *Sci. Rep.* **9** 4860 (2019).
12. H. Kalhori, M. Coey and I. A. Sarsari *et al.*, *Sci. Rep.* **7**, 12253 (2017).
13. L. Hu, G. Chen, X. Xie, *Journal of Materials Science & Technology* **33**, 569-582 (2017).
14. Z. Wang, L. Hu, G. Chen, *Nanoscale* **11**, 6748-6773 (2019).
15. Y. C. Chang, G. Chen, L. Hu, *Journal of Energy Chemistry* **59**, 322-336 (2021).
16. C. Wang, X. Zhu, *Journal of Materials Chemistry A* **5**, 18592-18611 (2017).
17. Y. Zheng, S. Ji, *ACS Applied Energy Materials* **1**, 1891-1914 (2018).
18. S. S. Sivathas, S. Murugan, A. V. Babu, S. Ramalingam, R. Thirumurugan, D. C. E. R. B. Victoria, *EUREKA: Physics and Engineering*, **4**, 101 (2022).
19. R. Lu, X. Zhong, S. Shang, S. Wang, M. Tang, *Royal Society Open Science*, **5**, 10 (2018).
20. Y. T. Heieh and M. W. Huang, *Thin Solid Films* **519**, 1668 (2010).
21. B. Cole, B. Marsen, E. Miller, Y. Yan, B. To, K. Jones and M. Al-Jassim, *J. Phys. Chem. C* **112**, 5213 (2008).
22. C.G. Granqvist, *Sol. Ener. Mater. Sol. Cells* **60**, 201 (2000).
23. C. Sella, M. Maaza, O. Nemraoui, J. Lafait, N. Renard, Y. Sampeur, *Surf. Coat. Tech.* **98**, 1477 (1998).
Thin Film Deposition by Spray Pyrolysis and the Application in Solid Oxide Fuel Cells
24. L. M. Bertus, A. Enesca and A. Duta ., *Thin Solid Films* **520**, 4282 (2012).
25. M. Kovendhan, D. Paul Joseph, E. Senthil Kumar, A. Sendilkumar, P. Manimuthu, S. Sambasivam, C. Venkateswaran and R. Mohan. *App. Surf. Sci.* **257**, 8127 (2011).
26. L. Lozzi, L. Ottaviano, M. Passacantando, S. Santucci, C. Cantalini, *Thin Solid Films* **391**, 224 (2001).
27. C. Cantalini, W. Wlodarski, Y. Li, M. Passacantando, S. Santucci, E. Comini, G. Faglia, G. Sberveglieri, *Sens. Actuators B* **64**, 182 (2000).
28. I. Porcheras and E. Betran, *Thin Solid Films* **377**, 129 (2000).
29. J. Livahe, G. Guzman, *Solid State Ionics* **84**, 205 (1996).
30. D. Ronnow, D. Kullman, C.G. Granqvist, *J. Appl. Phys.* **80**, 423 (1996).
31. C. Guillén, *Materials* **16**, 1359 (2023).
32. C. Guillén, *Advanced Energy Conversion Materials* **2**, 29 (2023).
33. J. Wang, J. M. Bell and I. L. Skryabin, *Sol. Energy Mater. Sol. Cell* **56** 465 (1999).
34. M. Rezagui, M. Addou, A. Outzourhit, J. C. Bernede, E. El Idrissi, E. Benseddik, A. Kachouane, *Thin Solid Films* **358**, 40 (2000).
35. M. Rezagui, M. Addou, A. Outzourhit, J. C. Bernede, E. El Idrissi, E. Benseddik, A. Kachouane, *Solar Energy Materials & Solar Cells* **77**, 341 (2003).
36. N. Gají, Ž. Kamberová, Z. Andí , J. Trpčevská, B. Plešingerová and M. Korać, *Open Access Metallurgy Journal* **9**, 277 (2019).
37. S. V. Mohite and K. Y. Rajpure, *Materials Science and Engineering B* **47** 47034951 (2015).
38. R. Abe, H. Takami, N. Murakami and B. Ohtani, *J. Am. Chem. Soc.* **130**, 7780 (2008).
39. M. Qamar, M.A. Gondal and Z.H. Yamani, *Catal. Comm.*, **11**, 768 (2010).
40. Dainius Perednis, *Thin Film Deposition by Spray Pyrolysis and the Application in Solid Oxide Fuel Cells*, Thesis, Zürich (2003).
41. D. Perednis and L. J. Gauckler, *Journal of Electroceramics* **14**, 103 (2005).
42. K. Jeyadheepan, P. Karthick and C. Sanjeeviraja, *JINST* **14**, P04002 (2019).
43. R. Sivakumar and A. E. R. Moses, B. Subramanian, M. Jayachandran, D. C. Trivedi, C. Sanjeeviraja, *Materials Research Bulletin* **39**, 1479 (2004).
44. N. Prabhu, S. Agilan, N. Muthukumarasamy, T. S. Senthil, *Int. J. ChemTech Research* **7**, 3492 (2014).
45. M. Xin, K.W. Li, H. Wang, *App. Surf. Sci.* **256**, 1436 (2009).
46. X. Zhang, B. Ren, X. Wu, X. Yan, Y. Sun, H. Gao and F. Qu, *ACS Omega* **39**, 25389 (2021).
47. N. W. Ashcroft, N. D. Mermin, (1976) *Solid State Physics*, (Cornell University, Harcourt Collage Publishers), pp. 24-27.
48. J. F. Owen, K. J. Teegarden and H. R. Shanks, *Phys Rev. B* **18**, 3827 (1978).
49. S. R. Bathe, P. S. Patil, *Solar Energy Materials & Solar Cells* **91**, 1097 (2007).
50. S. Dabbous. T. Nasrallah. J. Ouerfelli. K. Boubaker. M. Amlouk. S. Belgacem, *J. of All. and Comp.* **487**, 286 (2009).
51. Y. Sun, C. J. Murphy, K. R. R. Gil, E. A. R. Garcia, J. M. Thornton, N. A. Morris and D. Raftery, *int. j. hydr. energ.* **34**, 8476 (2009).
52. S. Chacko, M. J. Bushiri and V. K. Vaidyan, *J. of Phys. D: App. Phys.* **39**, 4540 (2006).
53. A. Sawaby, M. S. Selim, S. Y. Marzouk and A. Hosny, *Physica B*, 405, 3412 (2010).
54. D. G. Dickens and M. S. Wittingham, *Quart. Rev. Chem. Soc.* **22**, 30 (1968).

55. P. A. Lightsey, *Phys Rev. B* **8**, 3586 (1973). .
56. R. S. Crandall, B. W. Faughnan, *Phys Rev. Lett.* **39**, 232 (1977).
57. P. S. Patila, P. R. Patilb, E. A. Ennaouic, *Thin Solid Films* **370**, 38 (2000).
58. M. Gilleta, K. Aguirra, C. Lemirea, E. Gilleta, K. Schierbaumb, *Thin Solid Films* **467**, 239 (2004).
59. Y. Wang, X. Wang, Y. Xu, T. Chen, M. Liu, F. Niu, S. Wei and J. Liu, *small* **13** , 1603689 (2017).